Fatigue & Fracture of Engineering Materials & Structures

ORIGINAL CONTRIBUTION

doi: 10.1111/ffe.12220

Fracture of pearlitic ductile cast iron under different loading conditions

DIEGO O. FERNANDINO and ROBERTO BOERI

Metallurgy Division INTEMA, National University of Mar del Plata – CONICET, Mar del Plata, B7608FDQ, Argentina

Received Date: 17 December 2013; Accepted Date: 22 May 2014; Published Online: 13 June 2014

ABSTRACT In this study, fracture surfaces of pearlitic ductile iron generated under impact, bending and fatigue tests were characterised and compared. The fracture mechanisms in each case were identified from the observation of scanning electron microscopy images, and the characteristic topographic features were quantitatively and qualitatively evaluated. Cleavage was the predominant fracture mechanism for impact loading at all test temperatures and for slow bending testing. On the other hand, under fatigue loading, the fracture surfaces showed a mix of cleavage and ductile striation areas. A complex but reliable methodology for the determination of the direction of propagation of the main crack was also proposed, based on a careful analysis of the river patterns along the cleavage planes.

Keywords fracture surface; roughness parameters; fatigue; impact; bending; pearlitic ductile iron.

NOMENCLATURE

L' = Projected length of the fracture profile
Lt = Fracture profile length
Rs = Surface Roughness
Ry = Peak to valley ratio of the fracture profile
S_A = Projected surface area
St = Actual fracture surface area
V_i = Facet vector
M_i = Main vector
α_i = Angle between the local vector and the main crack propagation direction
β = Angle between the main vector and the main crack propagation direction

INTRODUCTION

Pearlitic ductile iron (PDI) has an excellent combination of high strength, toughness and wear resistance at low cost. The usual applications include gears, crankshafts, camshaft, dies, pistons, agricultural implement parts, ratchets, governor weights, truck shoes, tractor brake drums and mining machinery.[1] As ductile iron (DI) parts are extensively applied, failure events may take place, and it is essential to perform failure analyses to identify the causes of the fracture and to provide corrective actions to guarantee the safe operation. It is generally accepted that in the fracture process of a metallic material, the predominant fracture mechanisms can be revealed by identifying some characteristic features on the fracture surface.[2,3] For example, it has been established that the most common fracture mechanisms involved in metal fracture are ductile fracture, cleavage fracture, intergranular fracture and fatigue.[4–6] In general, the characteristic fractographic features of these fracture mechanisms are distinguishable by scanning electron microscopy (SEM) observations. The fractographic study is a fundamental tool for the failure analysis of a metallic part. When the materials used to make the parts are steel and other alloys, there is usually plenty of information about the correlation between the fractography and the type of loads that caused the failure. Nevertheless, when the fractured material is PDI, there is a noticeable lack of knowledge. In general, the research about PDI has been focused on the study of the mechanical properties using mechanical tests and qualitative microscopy techniques, but the fracture surface analysis was secondary.[7–13] Few authors have carried out quantitative studies of the fracture surface topography of samples of DI with different matrix microstructures.[14]

The aim of this work is to carry out a systematic study of the fracture surfaces of PDI under different loading conditions, in an attempt to correlate the features of the fracture surface with the acting loads, and to identify the crack propagation direction.

Correspondence: D. Fernandino. E-mail: dfernandino@fi.mdp.edu.ar

EXPERIMENTAL METHODOLOGY

Material characterisation

One inch 'Y' blocks of DI were cast in sand moulds (ASTM A897M) by MEGAFUND S.A. The chemical composition was determined by using a Baird DV6 spectrometer. Prismatic samples were machined from the Y blocks. Metallographic samples were prepared by using standard polishing and etching methods. Etching was carried out by using nital (2%). The microconstituents as well as the nodule count, nodularity and nodule size were quantified by using an optical microscope OLYMPUS PMG3 and the Image-Pro Plus software.

Mechanical testing

Brinell hardness measurements were carried out by using a universal testing machine 'Ibertest', Model 'DU-250' following the recommendations of the ASTM E10-01. The reported values are the average of at least three readings. V-notched Charpy impact specimens of 10 mm × 10 mm × 55 mm for impact and three-point bending test (ASTM E23) and SEN (B) specimens of 10 mm × 20 mm × 90 mm for fatigue test (ASTM E399) were machined from Y blocks (Fig. 1). The impact tests were performed by using a pendulum AMSLER 130/688, with a maximum energy of 300 J. To evaluate the effect of the test temperature on the fracture surface features, impact specimens were broken at four different temperatures. Three-point bending tests under quasistatic loading were performed by using a universal testing machine Morh&Federhaff with a cross-head displacement rate of 8.4×10^{-3} mm/s. For the fatigue test, SEN (B) specimens were broken using a displacement-controlled mechanical testing machine with a double eccentric actuator. A high cycle fatigue regimen was used. A maximum load of 2.2 kN approximately was applied using a constant eccentricity of $e = 0.145$ mm.[15] A stress ratio $R = 0$ was chosen for all tests. Stable crack propagation was attained following these conditions under small-scale plasticity. The frequency of the cyclic load was of 25 Hz. The specimens were identified as listed in Table 1.

Table 1 Summary of label used for each test conditions

Label	Matrix	Heat treatment	Test	Test temperature
PI-20	Pearlitic	As cast	Impact	−20
PI0				0
PI20				20
PI60				60
Pflx.			Bending	20
Pfat			Fatigue	20

Fracture surface and fracture profile

The fracture surfaces were examined by means of SEM to identify the predominant failure mechanisms.

The fracture profiles were characterised by optical microscopy. A schematic representation of the parameters used to characterise the roughness of the profiles is shown in Fig. 2. Each fractured sample was cut along a perpendicular plane to the v-notch and was mounted in bakelite and prepared for metallographic observation. The first cut was carried out using a metallographic cutting wheel under careful conditions to minimise plastic deformation. After cutting, samples were mounted in bakelite. The first grinding stage involved manual grinding for about 800 μm to remove any volume of metal that may have been affected by the cutting process. Fine polishing was then carried out. The five successive sections were obtained following a similar procedure, but using a shorter grinding time aimed at removing a layer of 500 μm approximately. These sections were uniformly distributed from the centerline. In all cases, the roughness parameters were measured along the stable crack propagation zone. The *Lt* value is the measurement of the actual length of the fracture profile whereas the L' value is the projected length of the fracture profile. For the numerical quantification of the surface roughness parameters, the Image-Pro Plus software was used. The results obtained were the average of 20 fields in five successive levels. Then, to define the roughness parameters of the fracture surface, the Underwood criteria was used.[16]

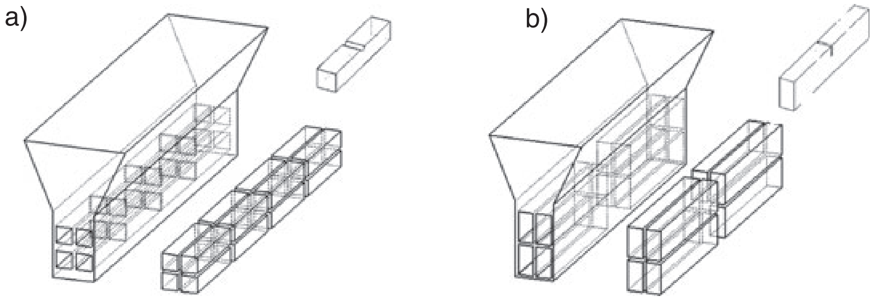

Fig. 1 Specimens machined from the Y blocks: (a) Charpy; (b) SEN (B).

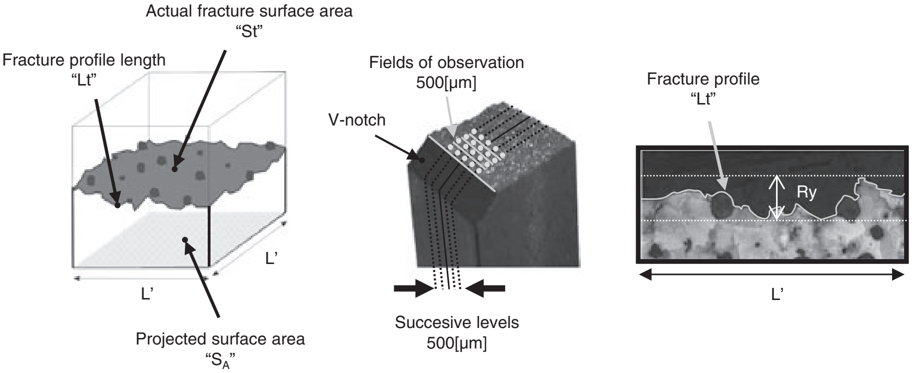

Fig. 2 Schematic representation of the roughness parameters.

Table 2 Chemical composition (Wt%)

C	Si	Mn	S	P	Mg	Cu	Ni	Cr
3.32	2.36	0.31	0.012	0.016	0.033	0.62	0.025	0.058

From the measurement of Lt and L' on the fracture profiles, Rl and Rs values were calculated, in each case, using Eqs (1) and (2), respectively. Rs is calculated as the ratio between the actual fracture surface area (S_t) and the projected surface unit (S_A) and gives a measure of the superficial roughness (Eq. (3)). In addition, the Ry values were obtained from the peak to valley ratio on the fracture profile (the difference between the height of the highest peak and the height of the deepest valley). These roughness parameters were also used by other authors to characterise the fracture surface and to compare the mechanical behaviour under varied test conditions both in metallic alloys[17–19] and in other composite materials.[20]

Table 3 As-cast characterisation

Label	Nodule count [nod/mm2]	Nodularity	Nodule size	Hardness
P	100	>95%	6	272 HB

As the number of measurements of a given variable is small, Student's t-distribution was applied to determine the values with a confidence interval of 95%.[21]

$$Rl\ [\mathrm{mm/mm}] = Lt/L' \tag{1}$$

$$Rs = (4/\pi)(Rl - 1) + 1 \tag{2}$$

$$Rs\ [\mathrm{mm^2/mm^2}] = St/S_A \tag{3}$$

RESULTS AND DISCUSSION

Chemical composition and microstructure

The chemical composition of the DI used is listed in Table 2. The as-cast microstructure characterisation according with the ASTM A 247 standard and the Brinell hardness are listed in Table 3. The nodularity was considered suitable for this study. The as-cast microstructure was 100% pearlitic and is shown in Fig. 3.

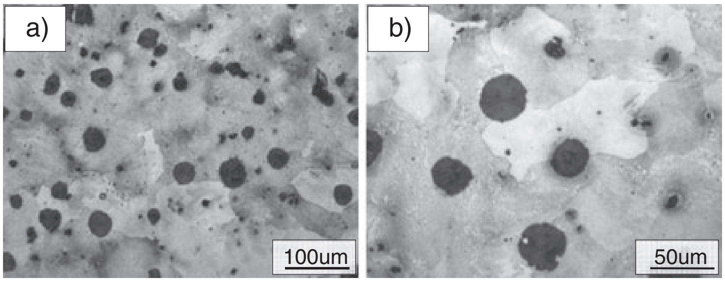

Fig. 3 As-cast microstructure. (a) 100x; (b) 200x.

Characterisation of fracture surfaces by SEM

The fracture surfaces resulting from impact loading at different temperatures are shown in Fig. 4. In general, exposed graphite nodules and nodular cavities free from graphite nodules (probably due to the detachment or total rupture of the nodule) were observed in all conditions. A brittle fracture surface conformed by cleavage facets that show river patterns and cracks that break into the surface (Fig. 4a) is characteristic in all samples. As the test temperature increases, the predominant fracture mode remains unchanged, and only a slight decrease in the number of cracks that break into the surface was found. Even for the samples tested at 60 °C, the nodular

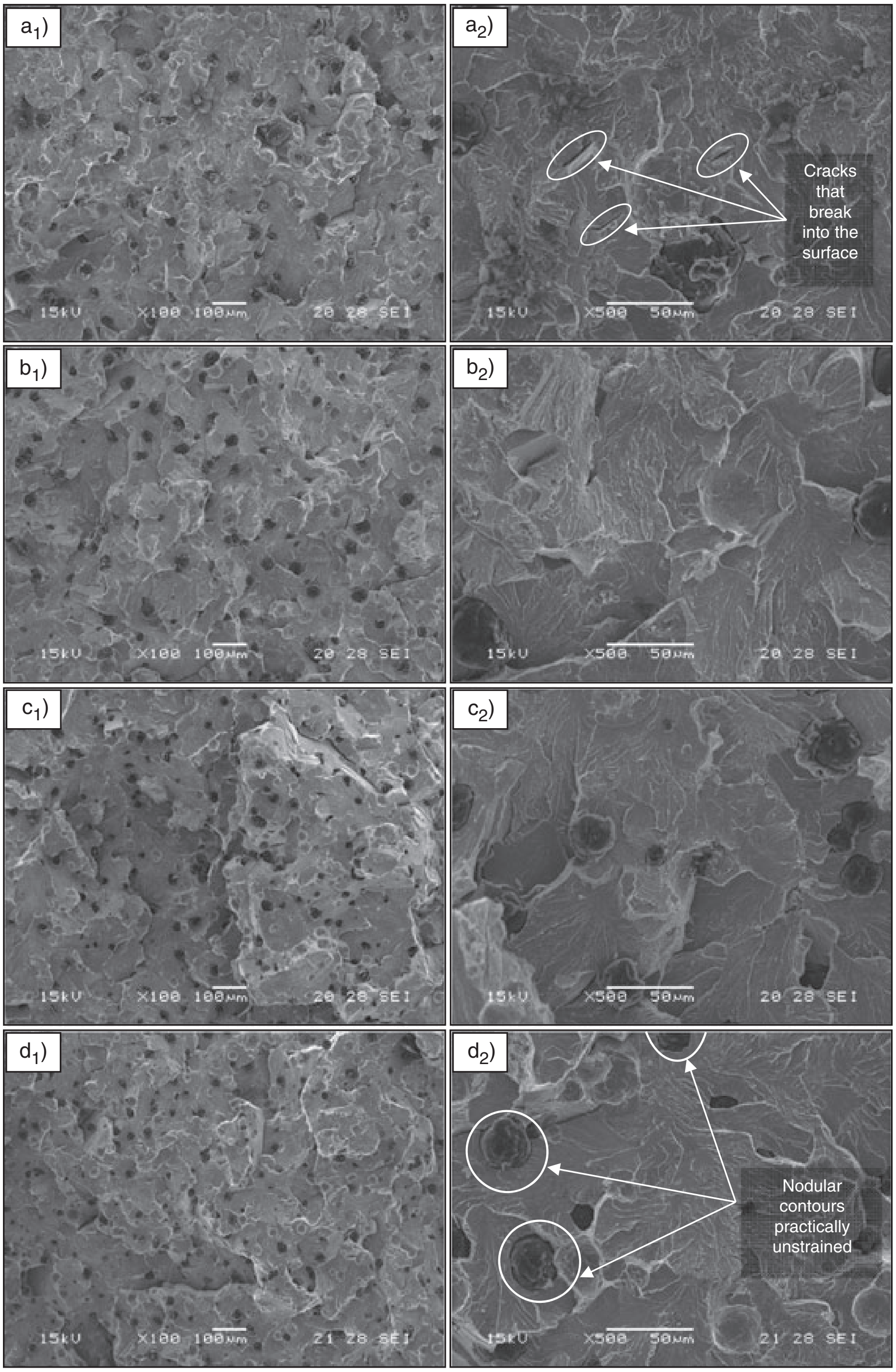

Fig. 4 Fracture surfaces from impact loads at different test temperatures. (a) −20 °C; (b) 0 °C; (c) 20 °C; (d) 60 °C.

contours showed little or no plastic strain (Fig. 4d). Only some very small ductile fracture regions were found both at high and low temperatures, as shown in Fig. 5. A mix of cleavage facets and ductile deformations feature was evidenced in all conditions.

The fractures surfaces from slow bending tests are shown in Fig. 6. As in the case of impact loading, brittle cleavage facets dominate the fracture surface. As is shown in Fig. 7, microplasticity in the cleavage steps and other zones was also identified. In consequence, in the same way that the results reported to impact test, brittle fracture was the predominant failure mode.

The fracture surfaces resulting from fatigue testing are shown in Fig. 8. Two different zones were evident for the naked eye on the surface: the unstable propagation zone

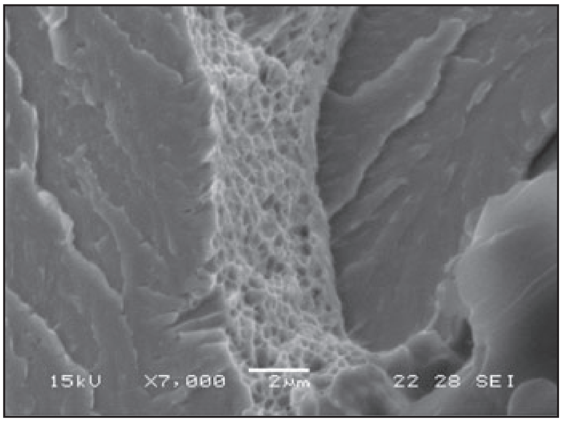

Fig. 7 Pflx sample. Microvoids formed in a cleavage step.

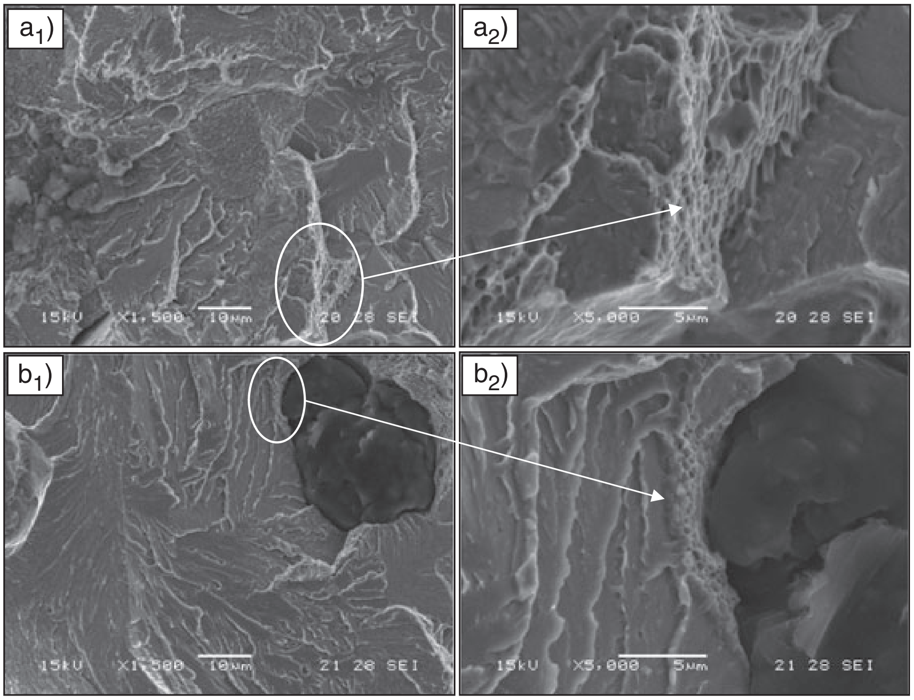

Fig. 5 Fracture surface from impact test. Different magnifications. (a) −20 °C; (b) 60 °C.

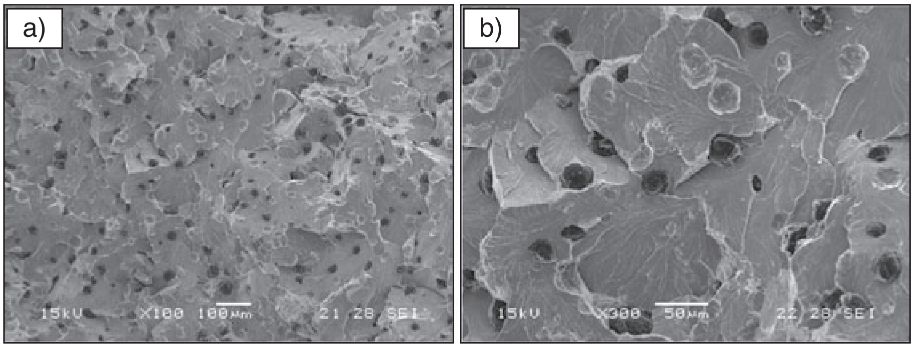

Fig. 6 Fracture surface from bending test. Different magnifications.

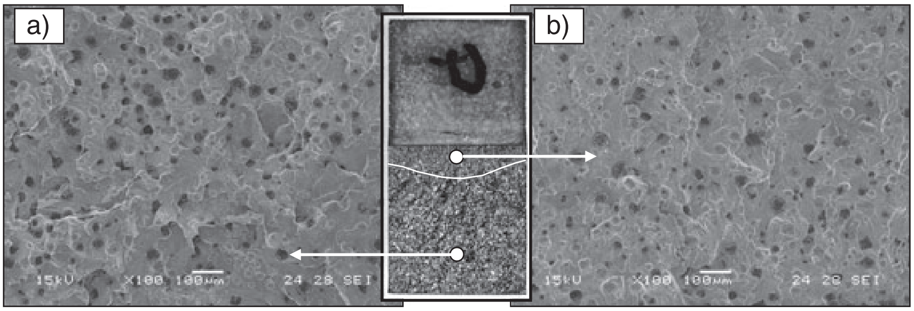

Fig. 8 Fracture surface from fatigue test. (a) Unstable propagation zone (final fracture); (b) Stable propagation zone.

(Fig. 8a) and the stable propagation zone (Fig. 8b). The unstable propagation zone showed the same features observed on the bending and impact test surfaces. In the stable propagation zone, where the crack actually propagates by fatigue, remarkable changes in the fracture surface were clearly distinguishable, as shown in Fig. 9. Signs of striation and a 'flatter topography' without deformation of nodular contours were observed. Cleavage facets mixed with areas showing striated features were observed in all fractographies. This feature was a predominant and distinctive characteristic of the fracture surfaces generated under cyclic loading (Fig. 9c and d). Secondary cracks and both ductile and fragile striations are the main fatigue crack propagation micromechanisms.

In Fig. 10, the fracture surfaces generated under impact, bending and fatigue test at room temperature are shown. The predominant fracture mechanism did not seem to change when the fracture surfaces from impact and bending test were compared. However, a noticeable change in the superficial topography was observed on the fracture surface from the fatigue test, and it allows to differentiate it from the other conditions.

Roughness of the fracture profile

The *Rs* and *Ry* values measured from the fracture profiles are shown in Fig. 11.

The roughness (*Rs*) of the fracture profiles from impact testing showed no significant change as a function of the testing temperature between −20 °C and 60 °C. On the other hand, when the fracture profile from the slow bending test is compared with that of the impact test

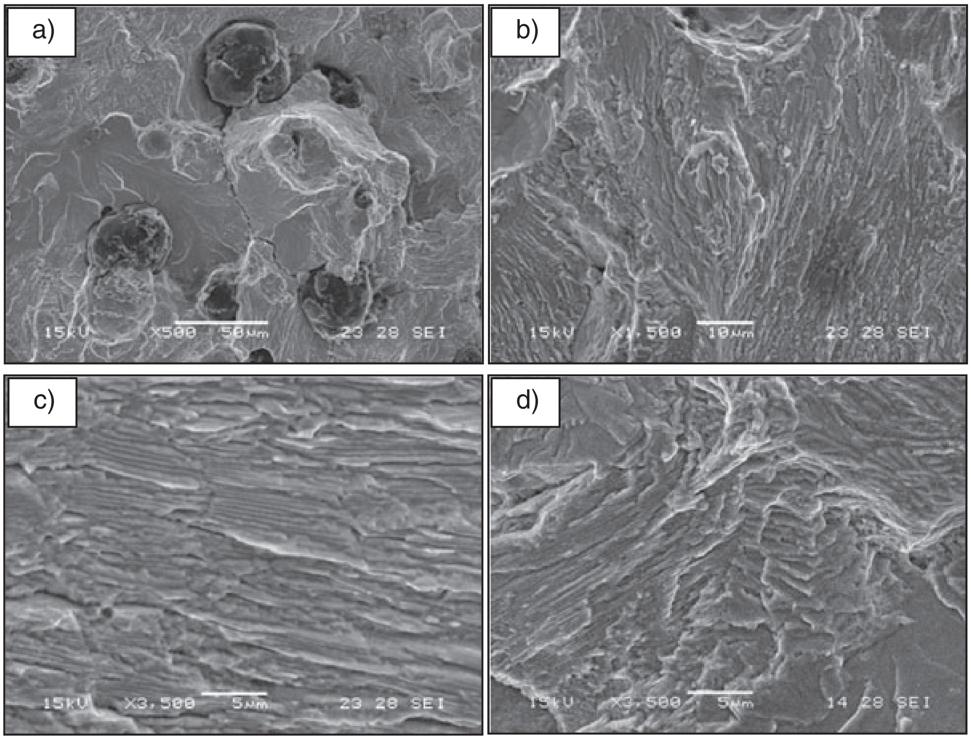

Fig. 9 Fracture surface from fatigue test.

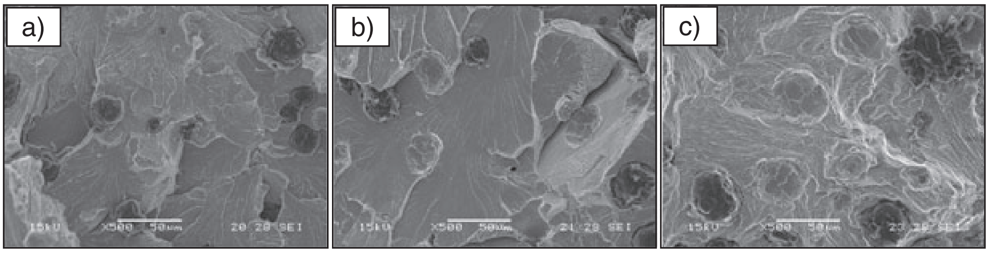

Fig. 10 Fracture surfaces tested at room temperature. (a) Impact; (b) bending; (c) fatigue.

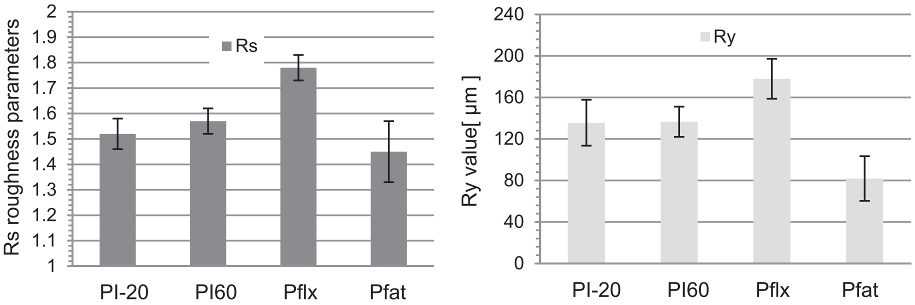

Fig. 11 Roughness parameter obtained by means impact, bending and fatigue test; (a) *Rs*; (b) *Ry*.

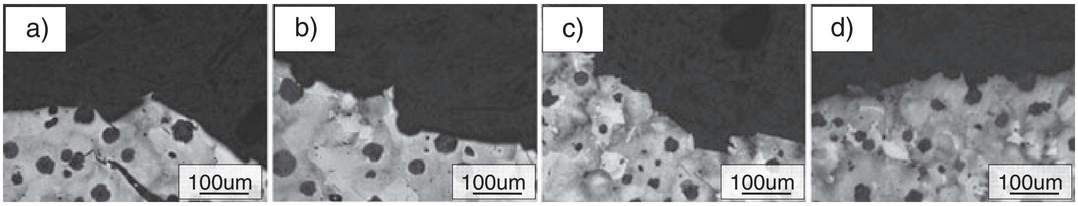

Fig. 12 Fracture profiles from impact, bending and fatigue testing. (a) PI-20; (b) PI60; (c) Pflx; (d) Pfat.

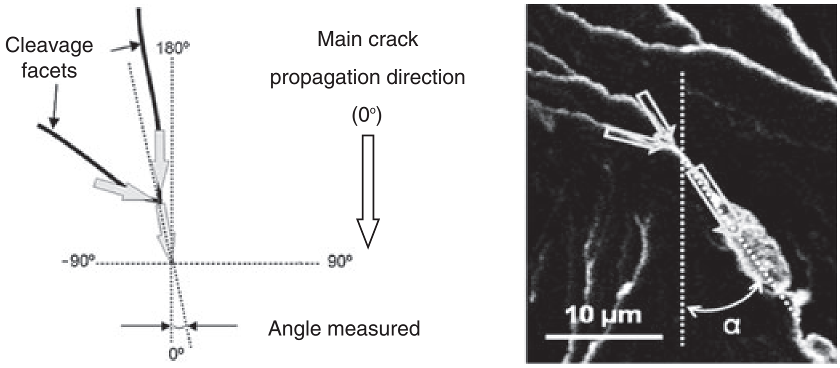

Fig. 13 Method used to define a local propagation vector on the cleavage fracture surfaces resulting of impact and bending test.

at 60 ºC, a clear increase in *Rs* is observed despite of the lower testing temperature (room temperature) used in the bending test. For fatigue fracture, *Rs* values are significantly lower than those measured for other loading conditions. Such changes in the fracture surface topography were clearly distinguishable by both SEM fractographies and optical fracture profiles. This noticeable decrease of the surface roughness value agrees with the results reported in the literature by other authors.[14] The values of *Ry* were also influenced by the test conditions (Fig. 11). As in the case of the *Rs* values, the measurements show no significant change as a function of the testing temperature of the impact test. On the other hand, an increase of *Ry* value in bending test as compared with impact test was observed. Similarly, a noticeable decrease of more than 50% was found for the fatigue fracture. The results indicate that different loading configurations on the same material lead to differences in *Rs* and *Ry* values of the fracture surface. This knowledge could be used to estimate the type of loading that leads to fracture in a fractographic analysis. Nevertheless, its application is at this point very limited because the influences of other features characteristic of the material microstructure, such as grain size and graphite size and morphology, are mostly unknown.

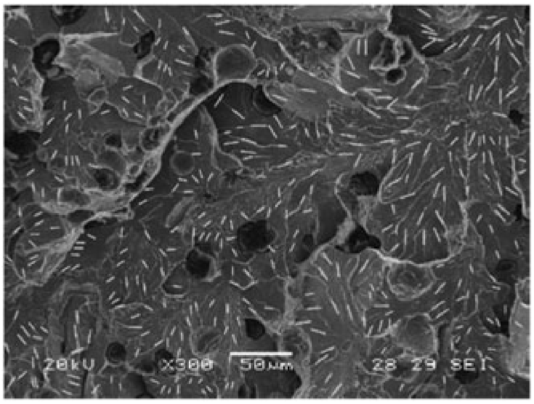

Fig. 14 Quantitative analysis on SEM fractographies by means Image-Pro Plus software. PI60.

Table 4 Statistical dataset obtained from the joint of each cleavage facet

	PI-20	PI60	PFlx
Mean	−5	3	−9
Media	−3	2	−10
Mode	0	0	0
Counts	1896	2416	2373

Representative micrographies of the fracture profiles of the impact (−20 °C; 60 °C), bending and fatigue test are shown in are shown in Fig. 12.

Direction of macroscopic propagation and its relation with the topographic features

Impact and slow bending fracture surfaces

As mentioned in Characterisation of Fracture Surfaces by SEM, in all samples tested by impact and slow bending loads, cleavage fracture was the dominant failure mode. The literature reports that the river patterns present on the cleavage facets converge into a single crack following the direction of the local crack propagation. Therefore, it should be possible to assess the main crack direction through the observation of the propagation on the cleavage planes or facets. The approach used was to identify and characterise the local propagation direction by means of observation of the directions of the river patterns with respect to the main crack propagation direction, which is known. Two different methodologies were applied. In all situations, the main crack propagation direction was set at 0° (Fig. 13).

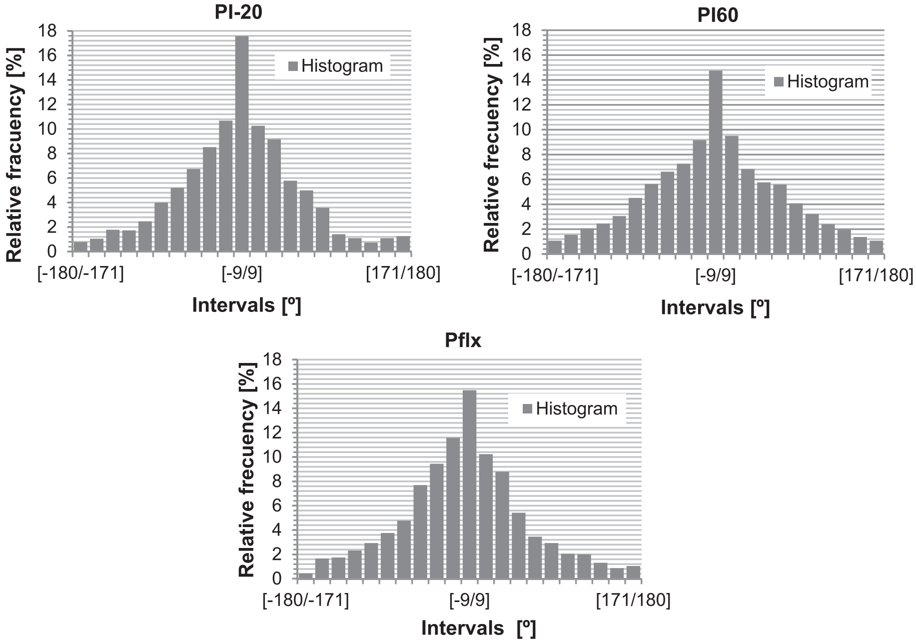

Fig. 15 Histograms from dataset.

Methodology 1. A local propagation vector was identified at the point in which two river patterns join, as shown in Fig. 13. All measured local propagation vectors were characterised by the angle formed with respect to the main crack propagation direction. The large number of values of local angles measured was averaged and the resulting direction compared with the main crack propagation direction.

An example of one of the SEM fractographies analysed for impact test at 60 °C is shown in Fig. 14. The results of the statistical dataset are listed in Table 4. In all cases, the mean (*X*) of the dataset was between −10° and 10°, and the mode value (*Mo*) of the distribution was 0°. These results not only show that the average of local propagation vectors reveals the predominant propagation direction, but also, at the local analysis, it was observed with higher relative frequency in this direction. For a better interpretation of the dataset, histograms of relative observation frequencies are also plotted in Fig. 15. The local directions were grouped into 20 intervals ranging from −180° to 180° in concordance with the reference system used in the present methodology.

Methodology 2. In the second methodology, the direction of the vectors formed by the joint of river patterns was measured as in method 1. However, in this case, all vectors belonging to the same cleavage facet were added, as shown in Fig. 16. The resulting vector for each facet is called 'facet vector' (V_i), and it is given a module magnitude proportional to the size of the facet area that it characterised ($|V_i| = A_i$). Later, a 'main vector' (M_i) is calculated as the resulting of the addition of the facet vectors, and its direction is characterised by the angle defined by the main vector with respect to the main crack propagation direction, called β. Figure 17 shows the calculated V_i for different cleavage facets present on a fracture surface. The values of the main vector direction resulting from the measurements of five fields of observation at 300× for each test conditions are listed in Table 5.

Table 5 shows that the largest difference between the main vector and the main crack propagation direction

Table 5 Results of methodology 2

	PI-20	PI60	Pflx
β [°]	−5	4	−8

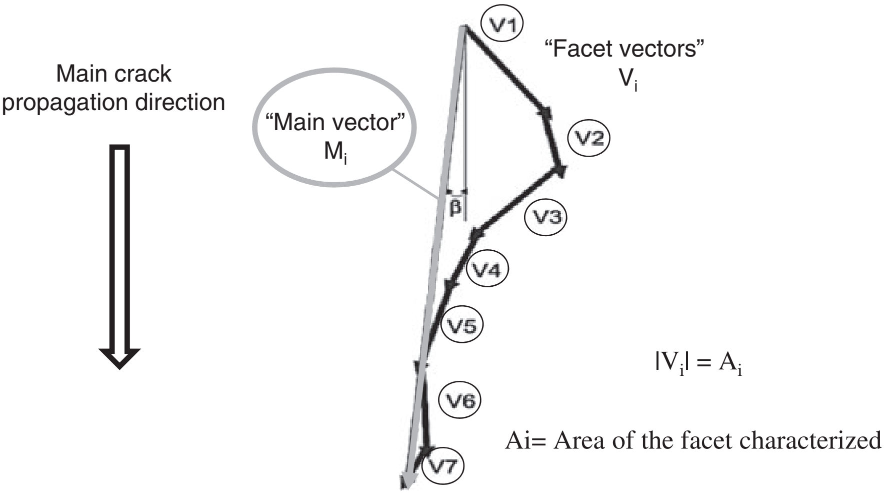

Fig. 16 Methodology to obtain the 'main vector' from the composition of each V_i.

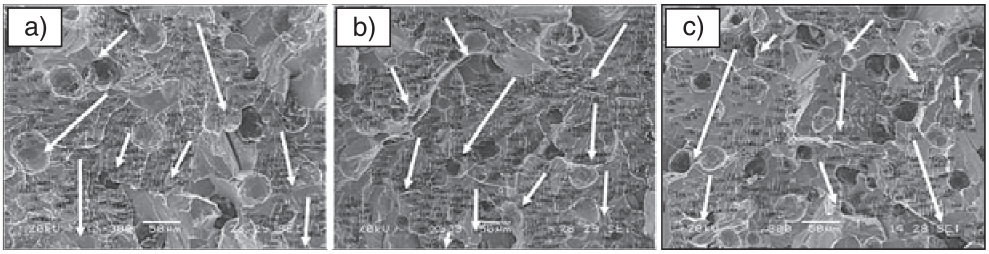

Fig. 17 Analysis of facet vector in each fracture surface; (a) PI-20; (b) PI60; (c) Pflx.

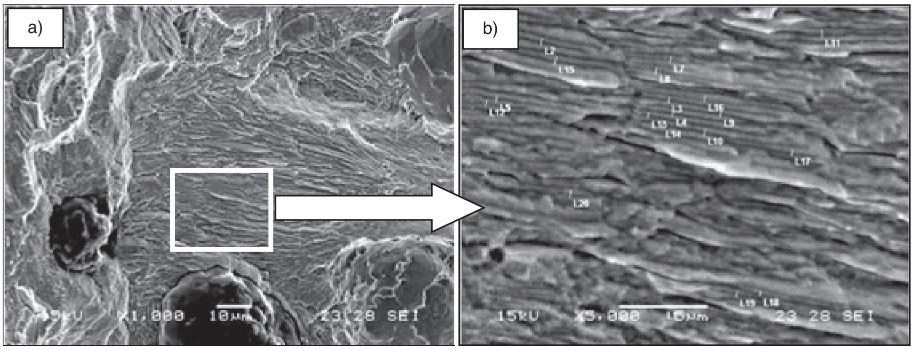

Fig. 18 SEM fractographies from fatigue test samples.

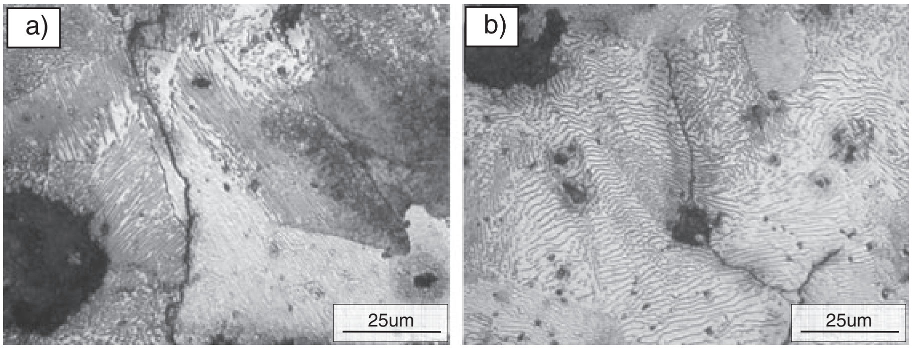

Fig. 19 Crack propagation path observed from the fatigue test. (a) Following the ferrite–cementite interface. (b) Across the pearlite lamellas.

was 8° for the bending test, in concordance with the results reported in Methodology 1. In consequence, both methodologies can be used to identify with very good accuracy the main crack propagation direction.

Fracture surfaces from fatigue

The characteristic features on the fracture surfaces from fatigue loading are shown in Fig. 18. It was not possible to find the classical striation marks or other features that may reveal the crack propagation direction. As reported in Characterisation of Fracture Surfaces by SEM, some areas on the fatigue fracture surfaces show lamellar features that could be at a first look taken as striation marks. Nevertheless, a closer look shows that the characteristic dimensions of the apparent striation marks are in concordance with the interlamellar distances of the pearlite (0.4 µm approximately). This similarity is shown in Figs 18 and 19. The crack propagation path during the stable crack propagation regime was observed interrupting the test, and the previously polished lateral surface of the sample was analysed at different times, to observe the microstructural zone chosen by the propagating crack. The propagating crack is not only seen to travel along ferrite–cementite interfaces at times but also observed to travel across the pearlite colonies. Therefore, no preferential orientation of the main crack path with respect of the pearlite lamellas was found, and no relation between fractographic features and the propagation direction was identified (Fig. 19).

CONCLUSIONS

The fracture surfaces of PDIs broken under impact, bending and fatigue loading were qualitatively and quantitatively characterised by analysing SEM and optical microscopy images.

- The fracture surfaces resulting from impact loading at different temperatures of PDI showed brittle fracture characteristics conformed by cleavage facets that show river patterns and cracks that break into the surface. Only some very small ductile fracture regions were found both at high and low temperatures.
- The fracture surfaces resulting from slow bending were similar to those observed after impact loading.
- The fracture surfaces resulting from fatigue showed some striation-like features. These features were not found on fracture surfaces generated under other loading conditions. Nevertheless, the striations have similar dimensions than the pearlite lamellas and show no

clear orientation along the fracture path. Therefore, observed striations could not directly be accounted for as fatigue striations.
- The roughness parameters *Rs* and *Ry* measured from the fracture profiles after optical microscopy were influenced by the loading conditions. The larger values corresponded to the slow bending conditions, followed by the impact fracture. The lower values were measured on the fatigue fracture.
- A method for the identification of the main crack propagation direction, based on a quantitative analysis of the river patterns present on the cleavage facets, was proposed. The method is applicable to impact and slow bending fracture surfaces. It identifies with very good accuracy the main crack propagation direction.
- No signs useful for identifying the direction of propagation of a fatigue crack in a PDI were found from the fractographic examination.

Acknowledgements

The authors are grateful to CONICET and the National University of Mar del Plata for their financial support and to MEGAFUND S.A. for the contribution with the castings used in this study.

REFERENCES

1 Burditt, F. M. (1992) Ductile Iron Handbook. American Foundrymen's Society, Inc., Des Plaines, Illinois, USA, pp. 31–36.

2 Davis, R. J. (1990) Metals Handbook, Vol. **11**, 9th edn, Failure Analysis and Prevention. American Society for Metals, Ohio, USA.

3 Fellows, A. J. (1973) Metals Handbook, Vol. **9**, 8th edn, Fractography and Atlas of Fractographs. American Society for Metals, Ohio, USA.

4 Anderson, T. L. (1995) Fracture Mechanics: Fundamentals and Applications, CRC Press, Boca Raton, Florida, USA, 2nd edn, pp. 265–305.

5 Barsom, J. M. and Rolfe, S. T. (1987) Fracture and Fatigue Control in Structures, Application of Fracture Mechanics, 2nd edn, Englewood Cliffs, New Jersey 07632 USA.

6 Broek, D. (1991) Elementary Engineering Fracture Mechanics, 4th edn, 101 Philip Dr., Kluwer Academic Publishers, Norwell, MA 02061 USA.

7 Iacoviello, F., Di Bartolomeo, O., Di Cocco, V. and Piacente, V. (2008) Damaging micromechanisms in ferritic-pearlitic ductile cast irons. *Mat. Sci. Eng. A*, **478**, 181–186.

8 Voigt, R. C. and Eldoky, L. M. (1986) Crack initiation and propagation in as-cast and fully pearlitic ductile cast irons. *AFS Trans.*, **94**, 637–644. Minneapolis, Minnesota; USA.

9 Hafiz, M. F., Hammouda, A. and El-Gemae, S. (2005) Impact properties and fractography of spheroidal graphite cast irons. *AFS Trans.*, 2–12. Schaumburg, II. USA.

10 Rajnovic, D., Eric, O. and Sidjanin, L. (2008) Transition temperature and fracture mode of as-cast and austempered ductile iron. *J. Microsc.*, **232**, 605–610.

11 Villacis Verdesoto, W. and Sikora, J. A. (1989) Crack initiation and propagation in spheroidal graphite cast iron with different micromorphologies. *Cast Met.*, **1**, 210–215.

12 Martínez, R. A. (2010) Fracture surfaces and the associated failure mechanisms in ductile iron with different matrices and load bearing. *Eng. Fract. Mech.*, **77**, 2749–2762.

13 Cavallini, M., Bartolomeo, O. and Iacoviello, F. (2008) Fatigue crack propagation damaging micromechanisms in ductile cast iron. *Eng. Fract. Mech.*, **75**, 694–704.

14 Bermont, V. M., Castillo, R. N. and Sikora, J. A. (2002) Fracture surfaces and mechanical properties in ductile iron. *ISIJ Int.*, **42**, 1303–1308.

15 Tada, H., Paris, P. C., Irwin, G. R. (2000) The Stress Analysis of Cracks Handbook, 3rd edn, American Society of Mechanical Engineers. ASME press, New York, USA, Part II.

16 Underwood, E. and Banerji, K. (1987) Metal Handbook, Vol. **12**, 9th edn, ASM, Metals Park, pp. 193–211.

17 Pokluda, J., Šandera, P. and Horníková, J. (2004) Statistical approach to roughness-induced shielding effects. *Fatig. Fract. Eng. Mater. Struct.*, **27**, 141–157.

18 Drar, H. and Svensson, I. L. (2006) Characterization of tensile properties and microstructures in directionally solidified Al-Si alloys using linear roughness index. *Mater. Charact.*, **57**, 244–258.

19 Dlouhý, I. and Strnadel, B. (2008) The effect of crack propagation mechanism on the fractal dimension of fracture surfaces in steels. *Eng. Fract. Mech.*, **75**, 726–738.

20 Ficker, T., Martišek, D. and Jennings, H. M. (2010) Roughness of fracture surfaces and compressive strength of hydrated cement pastes. *Cem. Concr. Res.*, **40**, 947–955.

21 Box, G. E. R., Hunter, W. G. and Hunter, J. S. (2005) Statics for Experimenters: an Introductions to Design, Data Analysis, and Model Building, 2nd edn, John Wiley & Sons, Inc., New Jersey.